Single-component multiphase lattice Boltzmann simulation of free bubble and crevice heterogeneous cavitation nucleation

Chi Peng,[1,2] Shouceng Tian,[1] Gensheng Li,[1,*] and Michael C. Sukop[2]

[1]*State Key Laboratory of Petroleum Resources and Engineering, China University of Petroleum-Beijing,*
18 Fuxue Road, Changping, Beijing, 102249, China

[2]*Department of Earth and Environment, Florida International University, 11200 SW 8th Street, Miami, Florida 33199, USA*

This work serves as an important extension of previous work on cavitation simulation [Sukop and Or, Phys. Rev. E **71**, 046703 (2005)]. A modified Shan-Chen single-component multiphase lattice Boltzmann method is used to simulate two different heterogeneous cavitation nucleation mechanisms, the free gas bubble model and the crevice nucleation model. Improvements include the use of a real-gas equation of state, a redefined effective mass function, and the exact difference method forcing scheme. As a result, much larger density ratios, better thermodynamic consistency, and improved numerical accuracy are achieved. In addition, the crevice nucleation model is numerically investigated using the lattice Boltzmann method. The simulations show excellent qualitative and quantitative agreement with the heterogeneous nucleation theories.

I. INTRODUCTION

Cavitation occurs when the local pressure falls below vapor pressure in liquid [1,2]. In acoustic (ultrasonic) cavitation, the local pressure fluctuation is induced by acoustic waves [3], while in hydrodynamic cavitation local pressure changes when flow passes through contraction-diverging sections such as throttling valves, nozzles, turbines, propellers, and hydrofoils [4–7]. Vapor cavities, called cavitation bubbles, will be formed and either grow or collapse depending on the ambient pressure of liquid. Cavitation is a ubiquitous phenomenon that has been recognized as a major source of erosion, noise, vibration, and efficiency degradation in hydraulic machinery [8]. Despite all the negative effects of cavitation, there has been growing interest in the application of cavitation as a positive tool and taking advantage of the high-pressure, high-temperature, microjet, and shock waves that result from cavitation bubble collapse. It has been shown that cavitation is able to improve drilling rate of petroleum wells [9], enhance heat transfer [10], dispose of wastewater [11], and conduct shotless peening [12], among others.

Numerous efforts have been advanced to figure out the mechanism and influence of cavitation. Due to the considerable cost of the experimental research on cavitation [13–18], numerical simulation of cavitation has long been pursued [19]. To solve the multiphase cavitation problem with conventional computational fluid dynamics (CFD) methods, both a Navier-Stokes equation and interface equation (such as volume of fluid [20] or level set method [21]) have to be solved simultaneously. Various numerical techniques, including finite element methods [22], finite volume methods [23–26], diffuse interface models [27], and two- [28,29] and three-dimensional [30,31] boundary element methods, have been employed to simulate

microscopic bubble behavior and macroscopic cavitation flows (e.g., cavitation jets and hydrofoil cavitation). However, even with simplified physical models (full cavitation model [32], Schner-Sauer model [33], and Zwart-Gerber-Belamri model [34]), which help to describe the liquid-vapor phase change, cavitation simulation using partial-differential-equation-based numerical methods is computationally demanding.

On the other hand, the lattice Boltzmann method (LBM), a mesoscopic CFD method based on kinetic particle dynamics and the Boltzmann equation, has displayed promising capability in the simulation of multiphase flows [35–39]. LBM has some intrinsic unique advantages such as easy implementation of boundary conditions, flexibility for complex boundary geometry, and ease of deployment in fully parallel algorithms [40]. The first multiphase LBM was proposed by Gunstensen *et al.* [41]. Since then different strategies for multiphase simulation have been suggested, which can be divided into four groups: the color-gradient model [41,42], free-energy model [43–45], kinetic-theory model [46,47], and pseudopotential model (Shan-Chen model) [48–51]. Because of its conceptual simplicity and computational efficiency, the pseudopotential model seems to be the most common model that receives large amounts of attention [37,38,50–56]. In the pseudopotential model, the interaction force between fluid particles is described by an interparticle potential, which is a function of local density. The separation of different phases (liquid and vapor) or of immiscible components is automatically realized, so interface capturing is no longer required.

The first attempt of applying LBM to the investigation of cavitation was made by Sukop and Or. [57]. Both homogenous and heterogeneous cavitation were simulated, and the evolution (growth or collapse) of single cavitation bubbles was presented, demonstrating the capability of LBM to simulate cavitation. Later Mishra *et al.* [58] successfully coupled the hydrodynamics of a collapsing cavitation bubble with solute chemical reactions using pseudopotential LBM. Chen

et al. [59] simulated cavitation bubble growth in a sheared liquid using pseudopotential LBM. The shape evolution of a cavitation bubble was found to be in good acordance with the theoretical prediction. Subsequently, Cheng *et al.* [60,61] developed a phase-change LBM that could simulate liquid-vapor phase change (boiling) by introducing a temperature component. Simulations of periodic bubble nucleation, growth, and departure from a heated wall were successfully realized. Falcucci *et al.* [62,63] simulated the flow-induced cavitation inside the nozzle of a cavitating injector using LBM with a nonideal equation of state. Daemi *et al.* [64] simulated the deformation and coalescence of a bubble cluster in an acoustic field using pseudopotential LBM. Kähler *et al.* [65] used LBM to investigate macrosropic cavitation inception near an orifice wall obstacle in a two-dimensional (2D) geometry. Subsequently, Yang *et al.* [66] and Shan *et al.* [67,68] used pseudopotential LBM to investigate cavitation bubble collapse near a solid boundary. The classic torus shape of a collapsing cavitation bubble was successfully obtained. Very recently, Sofonea *et al.* [69] successfully simulated bubble cavitation evolution in quiescent and sheared liquids using a third-order isothermal LBM coupled with van der Waals (vdW) equation of state (EOS).

In the present work, a modified pseudopotential single-component multiphase (SCMP) LBM is applied to simulate two heterogeneous cavitation nucleation processes. Special attention is paid to qualitative and quantitative comparisons between simulations and nucleation theories. In general, two important improvements are made that advance the previous work [57]. The first is the numerical method. The original Shan-Chen model used in Ref. [57] was plagued by a large spurious current, low attainable density ratio, and an artificial EOS that lacked a solid physical background. The density ratio between liquid and vapor was quite limited (only around 7) in Ref. [57]. In reality, the density ratio can easily exceed 100 for a liquid-vapor two-phase flow. Much effort has been expended to overcome the above-mentioned limitations [37–39,45,50–56,59–61,64–72]. Yuan *et al.* [37] redefined the effective mass function and managed to incorporate any real-gas EOS into LBM. Much larger density ratios were achieved, and thermodynamic inconsistency was reduced. Kupershtokh *et al.* [52] introduced the exact difference method (EDM) forcing scheme to the pseudopotential model, which was regarded as a significant enhancement for numerical stability and accuracy [53–55]. In this work, a real-gas EOS (Carnahan-Starling EOS) is used coupled with the EDM forcing scheme, which can achieve a density ratio more than 800. The second improvement corncerns the physcial model of cavitation nucleation. In the previous work [57], only free gas bubble nucleation was considered, while in this paper the crevice nucleation model will also be included. Heterogeneous nucleation is the initial condition for bubble cavitation in most cases since homogenous nucleation is extremely difficult [73,74]. In heterogeneous nucleation, free gas bubbles in liquid and gas trapped in solid crevices are the two most common sources of cavitation nuclei. The crevice model enjoys more universality. It proposes that small pockets of gas can stably settle at the bottom of cracks and crevices found on hydrophobic solid surfaces in contact with the liquid or on solid impurities that are widely present in liquid flows [75–79]. Overall, the

present work is intended to extend the scope of previous LBM cavitation simulations.

The rest of the paper is arranged as follows. Section II introduces the modified pseudopotential SCMP LBM. The thermodynamic properties of the model are addressed in Sec. III. Theoretical and numerical analysis of two heterogeneous cavitation nucleation models, free gas bubble and crevice nucleation, are presented in Sec. IV. The feasibility and validity of the current model for cavitation nucleation simulation will be tested based on the qualitative and quantitative comparisons between theoretical calculations and LBM simulation. Finally, a brief conclusion will be drawn in Sec. V.

II. MODIFIED PSEUDOPOTENTIAL SCMP LBM

As a mesoscopic method, LBM can be regarded as a fair approximation of the Navier-Stokes equations at macroscopic scale [36,38,40]. In LBM, the motion of fluid is described by a set of discrete single-particle density distribution functions. With the Bhatnagar-Gross-Krook approximation of the collision operator [80], the evolution equation of the density distribution function can be written as

$$f_\alpha(\mathbf{x} + \mathbf{e}_\alpha \delta t, t + \delta t) - f_\alpha(\mathbf{x}, t)$$
$$= -\frac{1}{\tau}\left[f_\alpha(\mathbf{x}, t) - f_\alpha^{\text{eq}}(\mathbf{x}, t)\right] + F_\alpha(\mathbf{x}, t), \quad (1)$$

where $f_\alpha(\mathbf{x}, t)$ is the density distribution function related to the discrete velocity direction $\alpha (\alpha = 0, 1, \ldots, N)$ at position $\mathbf{x}$ and time step t, N is the number of neighbor nodes, $\mathbf{e}_\alpha$ is the discrete particle velocity along the αth direction, δt is the interval of time step, τ is the relaxation time set as 1.0, $f_\alpha^{\text{eq}}(\mathbf{x}, t)$ is the equilibrium distribution function, and $F_\alpha(\mathbf{x}, t)$ is the source term that results from the external (gravity) and internal (adhesion or cohesion) forces.

Two kinds of particle operations, called streaming and collision, are implied in Eq. (1). In each time step, the left-hand side represents particle steaming from the original site $\mathbf{x}$ to the nearest neighbor sites $\mathbf{x} + \mathbf{e}_\alpha \delta t$, while the right-hand side represents the relaxation (collision) towards local equilibrium. After each time step, macroscopic density ρ and the velocity $\mathbf{u}$ are calculated by

$$\rho = \sum_{\alpha=0}^{N} f_\alpha, \quad \rho\mathbf{u} = \sum_{\alpha=0}^{N} \mathbf{e}_a f_a. \quad (2)$$

All the parameters are given in the form of lattice units: lengths are given in a lattice-based unit "l.u." that is equal to the lattice node spacing, mass is given in a lattice mass unit "m.u.," and time is given in a simulation time step "t.s."

In the present work, the D2Q9 lattice model with nine velocity directions on a 2D square lattice is used. So $N = 8$. The discrete velocity $\mathbf{e}_\alpha$ is expressed as

$$\mathbf{e}_\alpha = \begin{cases} (0, 0), & \alpha = 0 \\ c\left\{\cos\left[(\alpha-1)\frac{\pi}{2}\right], \sin\left[(\alpha-1)\frac{\pi}{2}\right]\right\}, & \alpha = 1-5, \\ \sqrt{2}c\left\{\cos\left[(2\alpha-1)\frac{\pi}{4}\right], \sin\left[(2\alpha-1)\frac{\pi}{4}\right]\right\}, & \alpha = 6-8 \end{cases}$$
$$(3)$$

where $c = \delta x / \delta t$ is the lattice speed, and lattice spacing δx and time step δt are set as unity, so $c = 1$l.u./t.s.

The equilibrium distribution function is calculated with

$$f_\alpha^{\text{eq}}(\mathbf{x}, t) = \omega_\alpha \rho(\mathbf{x}) \left[1 + 3\frac{\mathbf{e}_\alpha \cdot \mathbf{u}}{c^2} + \frac{9}{2}\frac{(\mathbf{e}_\alpha \cdot \mathbf{u})^2}{c^4} - \frac{3}{2}\frac{\mathbf{u}^2}{c^2} \right],$$

(4)

where the weighting coefficients ω_α are 4/9 for $\alpha = 0$, 1/9 for $\alpha = 1, 2, 3, 4$ and 1/36 for $\alpha = 5, 6, 7, 8$. c_s is the lattice sound velocity, and $c_s = \sqrt{c^2/3}$ in the D2Q9 scheme. The kinematic viscosity v is given by $\nu = c_s^2(\tau - 0.5)\delta t$ and is $1/6\,\text{l.u.}^2/\text{t.s.}$ in this paper.

Microscopically, the segregation of fluid into liquid and vapor is due to the interparticle forces. In SCMP LBM, a simple long-range interaction force between fluid particles at site $\mathbf{x}$ and $\mathbf{x} + \mathbf{e}_\alpha \delta t$ is introduced, which leads to spontaneous phase separation and transition. The boundary between liquid and vapor is displayed as a thin transition layer of several lattice units width where density swiftly changes from that of one phase to that of the other. The interaction force is given by

$$\mathbf{F}_{\text{int}}(\mathbf{x}) = -G\psi(\mathbf{x}) \sum_{\alpha=1}^{N} \omega_\alpha' \psi(\mathbf{x} + \mathbf{e}_\alpha \delta t)\mathbf{e}_\alpha,$$

(5)

where G reflects the intensity of the interparticle interaction, with $G < 0$ representing an attractive force and $G > 0$ representing a repulsive force between fluid particles. Effective mass $\psi(\mathbf{x})$ should be a monotonic function of density. To suppress spurious current, ω_α' is set as 1/3 for $\alpha = 1, 2, 3, 4$ and 1/12 for $\alpha = 5, 6, 7, 8$ according to the recommendation of Ref. [81].

In the original Shan-Chen model, the EOS of the system is derived from the predetermined $\psi(\mathbf{x})$ by

$$P = c_s^2 \rho + 0.5c_0 G \psi^2(\rho),$$

(5)

where P is the pressure and $c_0 = 6.0$ for D2Q9. Note that Eq. (5) has no corresponding physical meaning and is totally artificial.

In Ref. [37] a new scheme was proposed so that any kind of EOS can be used. Because of its ability to achieve wide temperature variation range and high density ratio, the Carnahan-Starling (C-S) EOS has been widely applied in the SCMP LBM simulation [53–55,59,67,68,70] and is chosen in this work. C-S EOS is given by

$$P = \rho RT \frac{1 + b\rho/4 + (b\rho/4)^2 - (b\rho/4)^3}{(1 - b\rho/4)^3} - a\rho^2, \quad (6)$$

where $a = 0.4963 R^2 T_c^2/P_c$, $b = 0.18727 RT_c/P_c$. We set $a = 1$, $b = 4$, $R = 1$, so the critical parameter is $T_c = 0.09433$, $P_c = 4.41644 \times 10^{-3}$, and $\rho_c = 0.13044$.

Equation (5) can be rewritten as

$$\psi(\rho) = \sqrt{2(P - c_s^2 \rho)/c_0 G},$$

(7)

and substituting P in Eq. (7) with Eq. (6) will lead to the ψ function based on C-S EOS. Other types of EOSs such as the vdW and Peng-Robinson (P-R) EOS can also be implemented because only the form of P needs to be changed according to the specific EOS. Note that in Eq. (7) G becomes unimportant because unlike in original Shan-Chen model, the temperature

is explicitly defined in Eq. (6). The only requirement on G is to ensure that the term under square root stays positive [37].

When investigating the crevice nucleation model, the adhesive force $\mathbf{F}_{\text{adh}}$ between fluid particle and solid surface needs to be incorporated to characterize the wettability effect. $\mathbf{F}_{\text{adh}}$ is given by [82]

$$F_{\text{ads}}(\mathbf{x}) = -G_{\text{ads}}\psi(x) \sum_{\alpha}^{N} \omega_\alpha s(\mathbf{x} + \mathbf{e}_\alpha \delta t)\mathbf{e}_\alpha,$$

(8)

where G_{ads} is the adsorption coefficient that represents the interaction strength between liquid and solid particles. $s(\mathbf{x} + \mathbf{e}_\alpha \delta t)$ is the indicator function expressed as

$$s(\mathbf{x} + \mathbf{e}_\alpha \delta t) = \begin{cases} 1, & \text{if } \mathbf{x} + \mathbf{e}_\alpha \delta t \text{ is solid particle} \\ 0, & \text{if } \mathbf{x} + \mathbf{e}_\alpha \delta t \text{ is liquid particle} \end{cases}.$$

(9)

The sum of all body forces $\mathbf{F}$ is defined as

$$\mathbf{F} = \mathbf{F}_{\text{int}}(\mathbf{x}) + \mathbf{F}_{\text{ads}}(\mathbf{x}) + \mathbf{F}_{\text{g}}(\mathbf{x}),$$

(10)

where $\mathbf{F}_{\text{g}}$ is the gravity, which is often neglected in the investigation of cavitation nucleation.

The next step is to incorporate $\mathbf{F}$ into the model. In the original Shan-Chen model, the velocity shifting method is used [48], where the interaction force is included as a change in the momentum during collision. This means $\mathbf{u}$ in Eq. (2) should be replaced by

$$\mathbf{u}^{\text{eq}} = \mathbf{u} + \frac{\tau \mathbf{F}(\mathbf{x})}{\rho(\mathbf{x})}.$$

(11)

and $F_\alpha(\mathbf{x}, t)$ is implicitly revealed in the change of $\mathbf{u}$.

However, the velocity shifting method will lead to the dependency of density ratio on relaxation time τ [52]. In comparison, the EDM forcing scheme can result in τ-independent densities and smaller spurious current [52–55], indicating better numerical stability. In EDM, the source term is given by

$$F_\alpha(\mathbf{x}, t) = f_\alpha^{\text{eq}}(\rho, \mathbf{u} + \Delta \mathbf{u}) - f_\alpha^{\text{eq}}(\rho, \mathbf{u}),$$

(12)

where $\Delta \mathbf{u} = \mathbf{F}\delta_t/\rho$ is the change of velocity due to body forces.

The real velocity $\mathbf{u}_{\text{real}}$ is obtained by averaging the moment before and after collision:

$$\mathbf{u}_{\text{real}} = \mathbf{u} + \frac{\tau \mathbf{F}(\mathbf{x})}{2\rho(\mathbf{x})}.$$

(13)

III. THERMODYNAMIC PERFORMANCE OF MODIFIED SCMP LBM

A. Coexistence curve of liquid and vapor

As a starting point, it is important to evaluate the modified model by comparing the coexistence curve obtained from the LBM simulations with the theoretical curve predicted by the Maxwell construction (the equal-area rule). To get the equilibrium densities for liquid and vapor at different temperatures, flat interface simulations are performed on an 80×80 square mesh with periodic boundaries in both the x and y directions. Half of the computational domain is initially filled with liquid, while the other half is filled with vapor. The
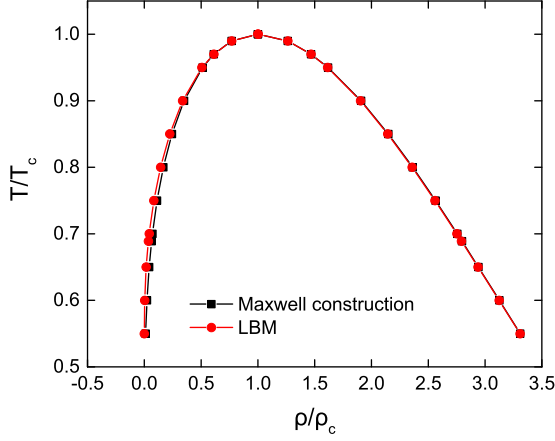
FIG. 1. Comparison of coexistence curve obtained from simulations with that obtained from Maxwell construction for a C-S EOS.

density field is initialized as

$$\rho(y) = \rho_{\text{vapor}} + \frac{\rho_{\text{liquid}} - \rho_{\text{vapor}}}{2} \left\{ \tanh\left[\frac{2(y-20)}{d}\right] \right.$$
$$\left. - \tanh\left[\frac{2(y-20)}{d}\right] \right\}, \tag{14}$$

where ρ_{liquid} and ρ_{vapor} are the equilibrium liquid and vapor densities derived from the Maxwell construction, and d is the initial interface thickness set as 5 l.u. The convergence criterion is

$$\frac{\sum_{x,y}^{D} |\rho_{x,y}(t) - \rho_{x,y}(t-1)|}{D^2 \sum_{x,y}^{D} \rho_{x,y}(t-1)} < 10^{-8}, \tag{15}$$

where D is the size of computational domain. This criterion applies to all the simulations in this paper and is sufficient to achieve the equilibrium state.

The result is given in nondimensional parameters in Fig. 1. The simulated coexistence curve satisfactorily fits the analytical curve, which shows good thermodynamic consistency with the present model. The largest relative error on the liquid density branch is only 0.26% found at $T/T_c = 0.8$. For the vapor branch, the relative error increases sharply with T decreasing from the critical value, although the absolute difference is still very small. This discrepancy between analytical and numerical vapor density may result from the compressibility effect or spurious currents in the peudopotential model [53]. Two major efforts have been made in present model to reduce spurious currents: (1) the use of the EDM forcing scheme [52–55] and (2) the optimal choice of ω'_α in Eq. (5) [81]. To further reduce the spurious currents, some major changes have to be made to improve the isotropy of the discrete gradient operator in SCMP LBM. When calculating the peudopotential, the number of lattice nodes involved can be increased from 8 (as in the current model) to 24 or even more. Details about these techniques can be found in Ref. [81]. When T is much lower than T_c, the density ratio between liquid and vapor becomes quite high. In the following simulations, an isothermal situation is assumed for microscopic cavitation phenomenon and T/T_c is set as 0.6. The corresponding equilibrium liquid and vapor density are 0.4059439 m.u./l.u.^{3} and 4.57075×10^{-4} m.u./l.u.^{3},
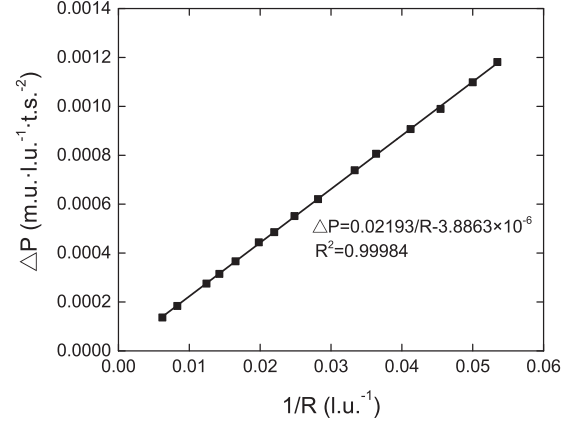

FIG. 2. Plot of curvature $(1/R)$ vs pressure difference used to determine the surface tension in a SCMP LBM.

respectively. The density ratio is nearly 10^3 (890), which approaches the magnitude of the density ratio of real water/water vapor flows (e.g., at 1 atmosphere pressure and 95 °C, the density ratio of water liquid to vapor is about 2×10^3).

B. Surface tension

The surface tension of the numerical SCMP LBM is obtained from simulations of vapor bubbles immersed in quiescent liquid, in which the pressure difference can be described by the Laplace law

$$\Delta P = P_{\text{in}} - P_{\text{out}} = \frac{\sigma}{R}, \tag{16}$$

where σ is the surface tension, P_{in} and P_{out} are the pressures inside and outside of the vapor bubble, and R is the bubble radius defined as the distance from the center of bubble to the interface where $\rho = 0.5(\rho_{\text{vapor}} + \rho_{\text{liquid}})$. The bubble simulations are conducted on a square domain that consists of 400×400 nodes. Periodic boundaries are applied in both directions. The central circular area is initialized with equilibrium vapor density, while the other part is initialized with equilibrium liquid density. The density field is initialized as

$$\rho(x, y) = \frac{\rho_{\text{liquid}} + \rho_{\text{vapor}}}{2} + \frac{\rho_{\text{liquid}} - \rho_{\text{vapor}}}{2}$$
$$\times \left(\left\{ \tanh \frac{2[\sqrt{(x-x_0)^2 + (y-y_0)^2} - R_0]}{d} \right\} \right), \tag{17}$$

where (x_0, y_0) is the center of the vapor bubble and $x_0 = y_0 = 200$, and R_0 is the initial radius of bubble ranging from 20 to 160 l.u. The variation of ΔP with $1/R$ is shown in Fig. 2. A conspicuous linear relationship is obtained. The numerical surface tension for vapor bubbles is 2.193×10^{-2} m.u./t.s.^{2} at $T/T_c = 0.6$. Liquid drops surrounded by vapor have also been simulated (not shown), and the corresponding surface tension is about 5% higher than that obtained from vapor bubbles. Considering that only vapor bubbles are simulated in the following sections, the surface tension measured from vapor bubble simulations is used to maintain consistency.
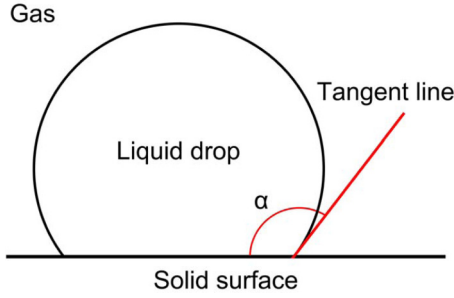
FIG. 3. Definition of contact angle of a liquid droplet on a solid surface.

C. Wettability

The wettability of a solid surface is directly related to the contact angle (α) of liquid droplet on it, which is defined as the intersection angle from the solid surface to the tangent line of the liquid-solid contact edge (Fig. 3). The smaller the contact angle is, the more hydrophilic the surface will be. In this model, wettability is decided by the adsorption coefficient G_{ads}. A series of simulations with varying G_{ads} is performed on a 200×200 domain. Periodic boundaries are applied in the x direction, while the top and bottom boundaries are set as no-slip walls. The density field is initialized as

$$\rho(x, y) = \frac{\rho_{liquid} + \rho_{vapor}}{2} - \frac{\rho_{liquid} - \rho_{vapor}}{2}$$
$$\times \left(\tanh \left\{ \frac{2[\sqrt{(x - x_0)^2 + (y - y_0)^2} - 50]}{d} \right\} \right),$$
(18)

where $x_0 = 100$ and $y_0 = 50$. Equation (18) defines a liquid droplet that is in contact with the bottom wall in the beginning. The adsorptive force will pull the liquid droplet closer to the wall, and the contact angle will be reached under equilibrium state.

Figure 4(a) shows the values of contact angle with different G_{ads}. It is fair to say that α is linearly proportional to G_{ads}, which accords with the results of Ref. [83]. It should be noted that the lowest achievable contact angle is $36°$ at $G_{ads} = -2.46$. Further decrease of G_{ads} will lead to severe numerical instability. The solid surface is fully hydrophobic when $G_{ads} > -0.9$. The shapes of liquid droplets in an equilibrium state with $G_{ads} = -1.2$ and -2.3 are given in Fig. 4(b) and 4(c). For $G_{ads} = -1.2$, the surface is strongly hydrophobic with α equal to $153°$. For $G_{ads} = -2.3$, the surface is hydrophilic with α equal to $52°$.

IV. THEORETICAL ANALYSIS AND NUMERICAL SIMULATION OF HETEROGENEOUS CAVITATION NUCLEATION

Based on the modified SCMP LBM, two popular theories of heterogeneous cavitation nucleation are examined in detail. Both qualitative and quantitative comparisons between simulation and theory are addressed. Besides the free bubble nucleation model, the crevice model is also investigated to complete the consideration of heterogeneous nucleation
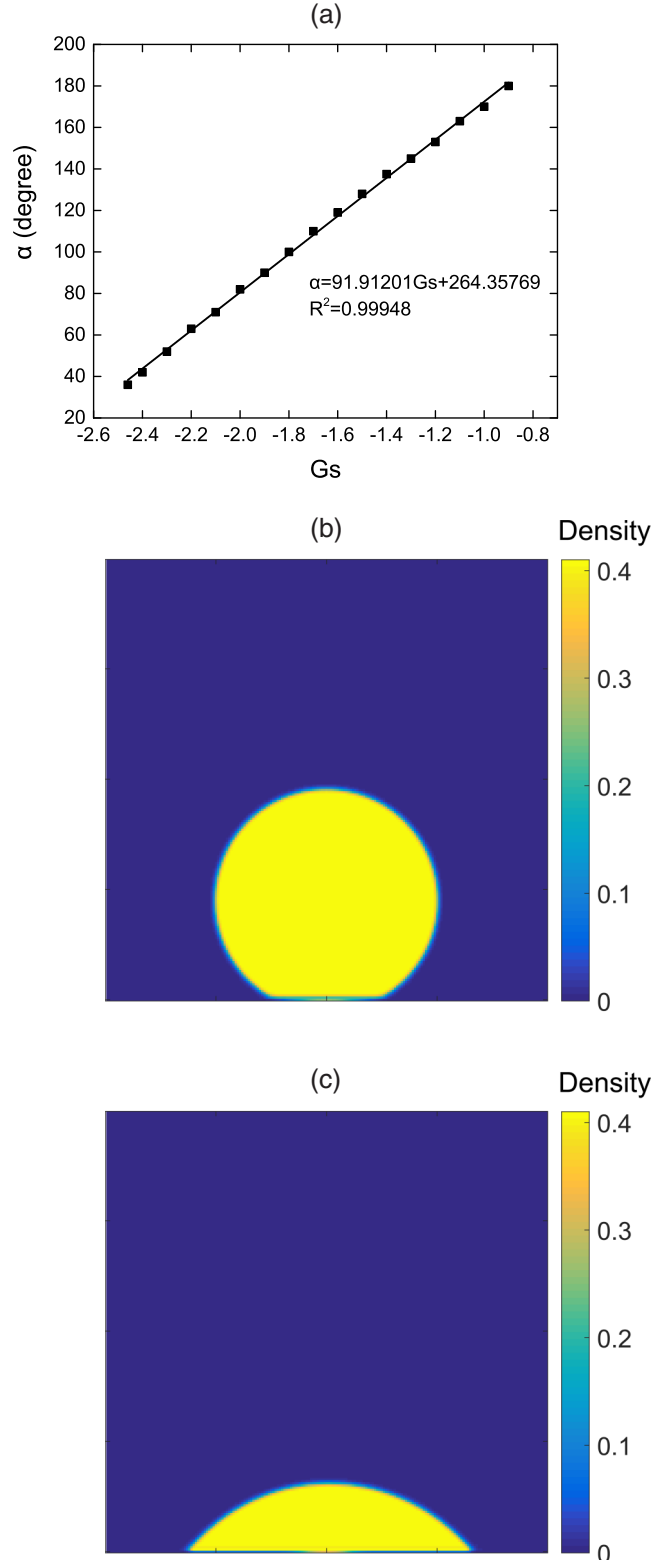

FIG. 4. Contact angles with different G_{ads}. (a) Plot of contact angle (α) vs G_{ads}; (b) equilibrium shape of the droplet with $G_{ads} = -1.2$ ($\alpha = 153°$); (c) equilibrium shape of the droplet with $G_{ads} = -2.3$ ($\alpha = 52°$).

theory. In reality, both free gas bubble and gas nuclei traped in crevices are likely to result in cavitation.

A. Free gas bubble nucleation

1. Theory

Free gas bubble nucleation occurs in liquid when a bubble of vapor or air acts as a seed for cavitation. Liquid under tension is metastable in that the formation and growth of a gas bubble can be more stable. However, an energy barrier ΔE must be overcome for the formation of a bubble, which equals the sum of the interfacial energy in the bubble surface and the work done by the gas and liquid pressure difference over the bubble volume [84]:

$$\Delta E = 4\pi R^2 \sigma + \tfrac{4}{3}\pi R^3 P_{\text{dif}}, \tag{19}$$

where $P_{\text{dif}} = P_{\text{liquid}} - P_{\text{vapor}}$.

In the 2D case considered here, Eq. (19) becomes

$$\Delta E = 2\pi R\sigma + \pi R^2 P_{\text{dif}}. \tag{20}$$

The maximum value of ΔE is attained when $\partial\Delta E/\partial R = 0$ and the corresponding bubble radius R_{cri} is

$$R_{\text{cri}} = -\frac{\sigma}{P_{\text{dif}}}. \tag{21}$$

Equation (21) defines a critical bubble radius. That is, at a specific P_{dif}, a bubble whose radius is less than R_{cri} will condense rather than cavitate because condensation is preferable in terms of lowering system energy. The vapor bubble will continuously shrink and finally disappear. In contrast, if a bubble is larger than the critical size, cavitation becomes more favorable and the bubble will grow without limit due to evaporation of liquid nearby. The phase trasition is spontaneous as long as P_{dif} permits it. On the other hand, Eq. (21) can also be usd to predict what critical liquid tension should be exceeded to initiate the cavitation process for a preexisting bubble of a particular radius.

The size change of a bubble, either its shrinkage or growth, can be described by the classic Rayleigh-Plesset equation, which was originally derived for the evolution of a spherical gas bubble in infinite liquid [19,85,86]:

$$R\ddot{R} + \frac{3}{2}\dot{R}^2 + \frac{4\nu}{\rho_{\text{liquid}} R}\dot{R} + \frac{2\sigma}{\rho_{\text{liquid}} R} = \frac{P_B - P_\infty}{\rho_{\text{liquid}}}, \tag{22}$$

where P_B is gas pressure inside the bubble and P_∞ is the liquid pressure at infinite distance.

In the present 2D simulation, the Rayleigh-Plesset equation should be revised as [69,70]

$$\ln(R_{\text{bound}}/R)(\dot{R}^2 + R\ddot{R}) - \frac{1 - (R/R_{\text{bound}})^2}{2}\dot{R}^2 - \frac{2\nu}{\rho_{\text{liquid}} R}\dot{R}$$

$$+ \frac{\sigma}{\rho_{\text{liquid}} R} = \frac{P_{\text{vapor}} - P_{\text{bound}}}{\rho_{\text{liquid}}}, \tag{23}$$

where R_{bound} is the size of the square domain, R is the radius of the 2D bubble, P_{vapor} is the pressure inside the gas bubble (simplified as the vapor pressure), and P_{bound} is the pressure defined at the model boundaries. All the parameters in Eq. (23) will be set as the same used in LBM simulations. At $t = 0$ t.s. the first derivative of R is 0 l.u./t.s. Eq. (23) is numerically solved using a Runge-Kutta method and is used to quantitatively verify the LBM simulation of free gas bubble nucleation behavior in the next section.

2. Simulations and results

The simulations of free bubble nucleation are conducted on a 400×400 domain with $T/T_c = 0.6$. In order to have better accordance with the realistic physical situation, pressure boundaries are used at all four edges. The pressure boundaries are implemented using the standard approach described in Ref. [87], similarly to previous studies on cavitation bubble LBM simulation [57–59,66,70]. Note that in Ref. [57] pressure boundaries were only applied on the top and bottom edges (y direction), while periodic boundaries were used on the left and right edges. The inconsistant application of boundary condition is the reason for the noncircular shape of cavitation bubbles in Figs. 4 and 5 of Ref. [57]. The full pressure boundaries allow the cavitation bubble to maintain a perfectly round shape except for the later stage of growth (when bubble radius is larger than 150) where the limited size of the computational domain restricts the free deformation of the bubble. The density field is initialized according to Eq. (17).

A series of SCMP LBM simulations with various bubble intial radii R_{inital} and P_{dif} were conducted. The validation of the critical radius for bubble nuclei to cavitate is shown in Fig. 5. At $P_{\text{dif}} = -5.90 \times 10^{-4}$ m.u. l.u.$^{-1}$ t.s.$^{-2}$, R_{cri} is equal to 37.2 l.u. A bubble whose initial radius is just below R_{cri} cannot overcome the energy barrier for cavitation. It will shrink and eventually disappear [$R_{\text{inital}} = 35.5$ l.u., Fig. 5(a)]. However, a seed bubble with radius just above R_{cri} will induce cavitation [$R_{\text{inital}} = 40.5$ l.u., Fig. 5(b)]. Note that in the early stage of bubble evolution the change of radius is almost undetectable so R at $t = 50$ and 100 t.s. is equal to R_{inital}. Figure 6 shows the effect of pressure difference for a bubble with $R_{\text{inital}} = 50.5$ l.u. The critical P_{dif} for caivitation is -4.34×10^{-4} m.u. l.u.$^{-1}$ t.s.$^{-2}$. When P_{dif} is larger than the critical value, the seed bubble cannot meet the energy requirement and collapses [$P_{\text{dif}} = -3.46 \times 10^{-4}$ m.u. l.u.$^{-1}$ t.s.$^{-2}$; Fig. 6(a)]. Only when P_{dif} is smaller than the critical value will cavitation happen [$P_{\text{dif}} = -4.83 \times 10^{-4}$ m.u. l.u.$^{-1}$ t.s.$^{-2}$; Fig. 6(b)].

As shown in Fig. 7, in both cases where P_{dif} and R_{inital} are separately kept constant, very good agreement has been achieved between simulations and Eq. (23). The existence of a critical radius and critical pressure difference is conspicuous. Generally speaking, in cases of bubble growth (cavitation), SCMP LBM simulations tend to predict faster bubble expansion than the revised Rayleigh-Plesset equation in the early stage of bubble growth. However, in late stage of bubble growth, expansion is greatly affected by the limited domain size and thus becomes slower than the revised Rayleigh-Plesset equation prediction. On the contrary, in cases of bubble collapse (condensation), SCMP LBM simulations often predict slower bubble shrinkage than Eq. (23). This inconsistency may come from the fact that both liquid and vapor phase share the same kinematic viscosity ν in LBM simulations, while in Eq. (23) the viscosity of vapor is ignored. Overall, a satisfying accordance is obtained, which elucidates the validity of the modified SCMP LBM to quantitatively investigate bubble dynamics during free bubble cavitation nucleation process.

B. Crevice nucleation model

In free bubble nucleation theory, under a specific pressure condition only bubbles with identical size can exist. However,
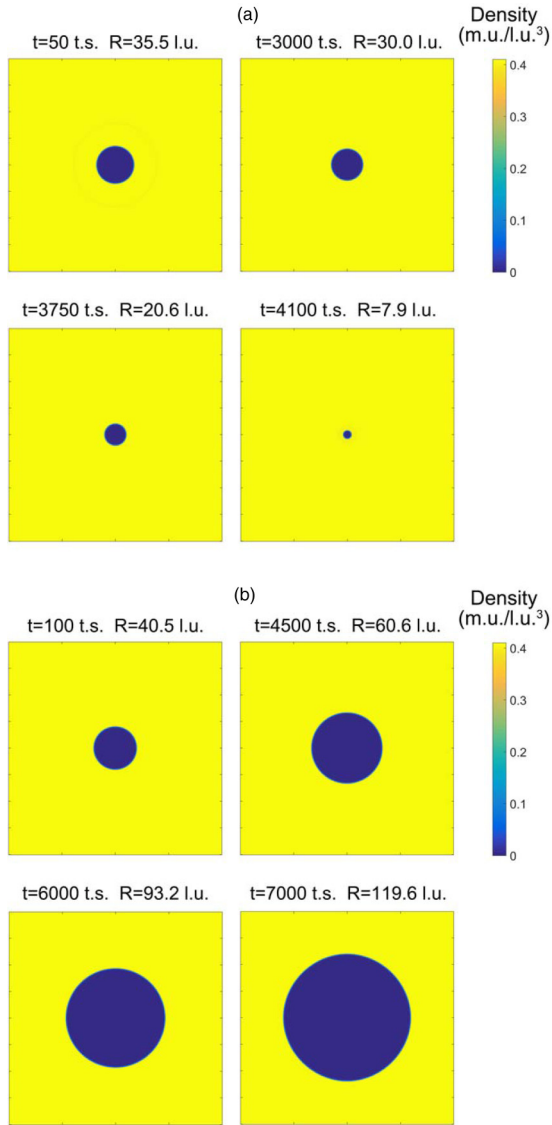
FIG. 5. Effect of initial bubble size on bubble evolution for $P_{\text{dif}} = -5.90 \times 10^{-4}$ m.u. l.u.$^{-1}$ t.s.$^{-2}$. (a) $R_{\text{inital}} = 35.5$ l.u. Seed bubble shrinks due to condesation; (b) $R_{\text{inital}} = 40.5$ l.u. Seed bubble grows due to evaporation.

FIG. 6. Effect of pressure difference on bubble evolution for $R_{\text{inital}} = 50.5$ l.u. (a) $P_{\text{dif}} = -3.46 \times 10^{-4}$ m.u. l.u.$^{-1}$ t.s.$^{-2}$. Seed bubble shrinks due to condesation; (b) $P_{\text{dif}} = -4.83 \times 10^{-4}$ m.u. l.u.$^{-1}$ t.s.$^{-2}$. Seed bubble grows due to evaporation.

this deviates from the experimental fact that gas bubbles whose radii range between several to hundreds of micrometers can coexist in the same liquid [88,89]. An extra mechanism is needed to explain the discrepancy. For example the varying-permeability model assumes a skin of surrounding surface active molecules helps to stabilize the gas bubble [90,91]. In contrast, the crevice nucleation model is self-adaptive and enables the mechanical stability of gas nuclei with various sizes.

1. Theory

In reality, liquid such as water normally contains a large number of solid impurities suspended in it. These impurities characteristicly have an irregular surface marked by deep grooves, crevices, and pits [92–94]. The surface is frequently
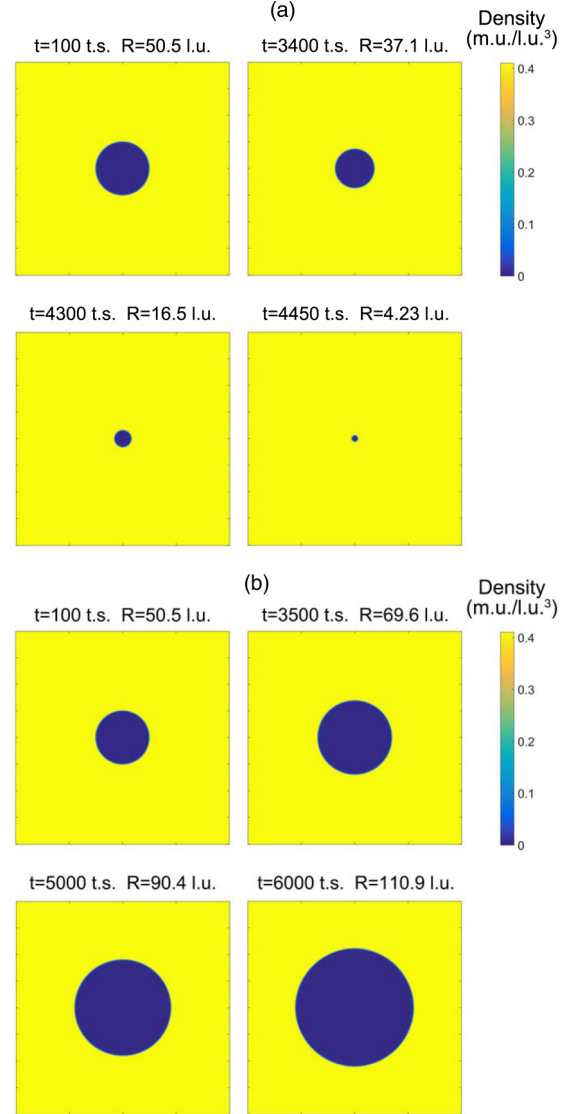
hydrophobic because of the material itself and consequently, some gas can remain entrapped at the bottom of the crevices when the impurities contact the fluid [75,77]. An example of the idealized crevice nucleation model is shown in Fig. 8. The crevice is 2D conical with a half-angle aperture β. W_{m} is the half-width of the crevice mouth while W is the half-width of a generic two phase interface. R is the radius of curvature and α is the contact angle. The gas nucleus is stabilized when the balance of force is achieved:

$$P_{\text{vapor}} + \frac{\sigma}{R} = P_{\text{liquid}}, \tag{24}$$

and the following geometrical requirement is satisfied:
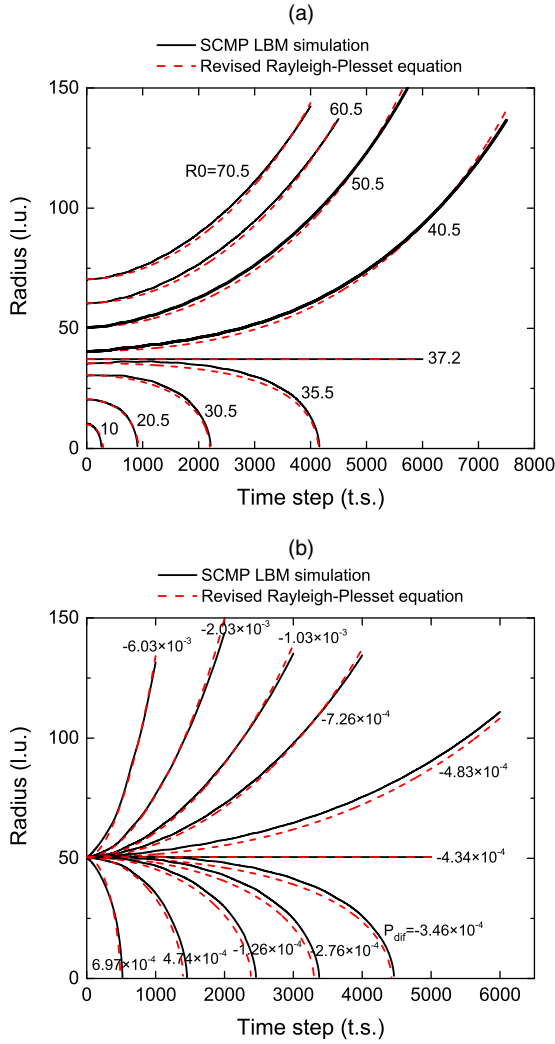
$$W = R|\cos(\alpha - \beta)|. \tag{25}$$

FIG. 7. The comparison of bubble size evolution between SCMP LBM simulation and revised Rayleigh-Plesset equation predictions. (a) P_{dif} is kept at -5.90×10^{-4} m.u. l.u.$^{-1}$ t.s.$^{-2}$. Corresponding R_{cri} is 37.2 l.u.; (b) R_{inital} is kept at 50.5 l.u. Critical P_{dif} for caivitation is -4.34×10^{-4} m.u. l.u.$^{-1}$ t.s.$^{-2}$.

So in theory, the half-width of the generic interface should be

$$W = \frac{\sigma}{P_{\text{dif}}} |\cos(\alpha - \beta)|. \tag{26}$$

Equation (26) will be used to validate the simulation results. One difference between the free bubble nucleation and crevice nucleation is the role of surface tension. In the free bubble case, the interface of gas and liquid must be convex towards the liquid, meaning surface tension always helps to squeeze the gas bubble and must be counterbalanced by the pressure difference. In crevice nucleation, the interface is convex towards the gas so that surface tension actually helps to stabilize gas nuclei against liquid pressure.

2. Simulations and results

The simulations of crevice nucleation are also conducted on 400×400 domain with $T/T_c = 0.6$. Based on the crevice
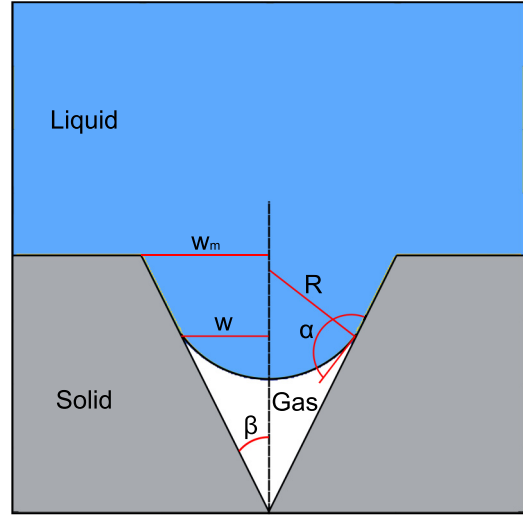

FIG. 8. The idealized crevice nucleation model with a conical crevice of half-angle β and mouth width w_m in a hydrophobic solid particle.

nucleation theory, pressure boundaries [87] are used at the top, left, and right edges to maintain a constant P_{liquid} in each simulation. The bottom boundary (solid surface) is set as a no-slip bounce-back wall. For each combination of crevice shape and contact angle, the density field is initialized with Eq. (17), where $x_0 = 200$, $y_0 = 1$, and $R_0 < W_m$. The convergence criterion is the same as in Eq. (15). If the liquid pressure is properly defined, a stable state can be attained with the vapor phase resides in the crevice [like the first three figures of Fig. 9(a)]. After one stable state is attained, the boundary pressure can be either increased or decreased to achieve other states. Crevices with different shape (β) and surface wettability (α) are investigated.

If liquid pressure continuously increases (P_{dif} increases), a preexisting vapor nucleus will gradually recede to the apex of crevice and eventually vanish [Fig. 9(a)]. This means vapor nuclei in a crevice will be eliminated due to pressurization. In engineering applications, pressurization is a widely used method to suppress cavitation. On the contrary, if liquid pressure keeps falling (P_{dif} decreases), once the critical condition is surpassed a vapor nucleus cannot rearrange itself to a stable state in the crevice. The interface will change from being convex towards the vapor to concave towards the vapor, and the nuclei will grow and move out the crevice [Fig. 9(b)], leading to cavitation.

The effect of crevice shape (β) on nuclei is shown in Fig. 10. Under the same liquid pressure, the narrower the crevice is, the more space the vapor phase occupies and the closer the vapor is to the crevice mouth. This means that a narrower crevice is more favorable for cavitation. On the other hand, wider crevice will be the first to lose its nucleus and become an inactive nucleation site during the pressurization process. This trend agrees with the crevice nucleation theory [75,79,95]. According to Eq. (24), at fixed P_{liquid}, the curvature radius R should be the same regardless of crevice geometry. This is verified by the red dash-line circles with the same radius in Fig. 10 that depict R for each crevice.
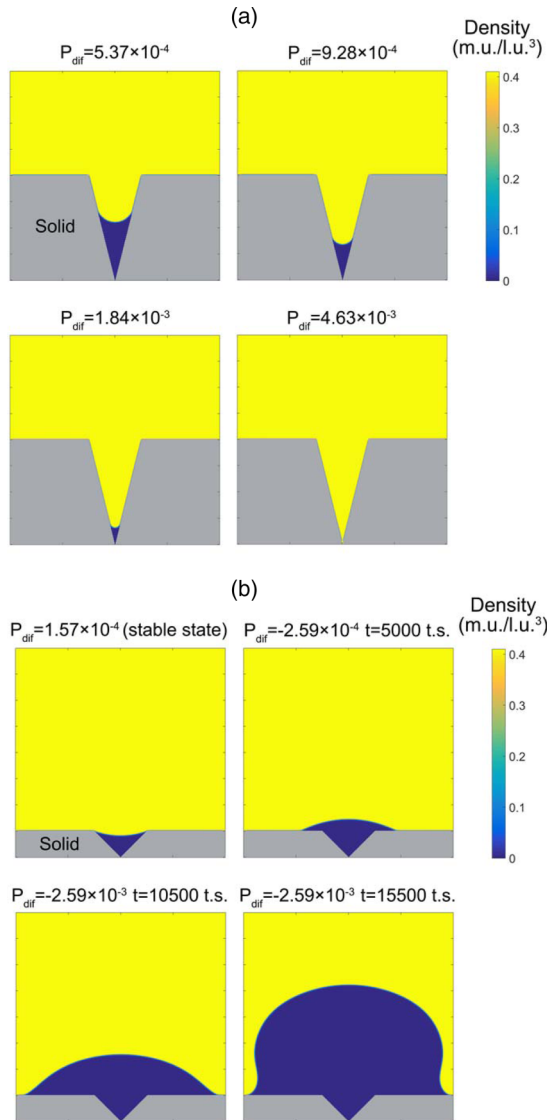
FIG. 9. The change of vapor nuclei under different P_{dif} (unit: m.u. l.u.$^{-1}$ t.s.$^{-2}$). (a) $\alpha = 170°$, $\beta = 26.55°$, vapor nucleus is suppressed due to pressurization; (b) $\alpha = 163°$, $\beta = 45°$, vapor nucleus grows out of crevice due to cavitation.

The effect of crevice surface wettability (α) on nuclei is shown in Fig. 11. Again, at the same P_{liquid} the curvature radius is the same regardless of α. However, interface half-width W will decrease with smaller α, as shown by Eq. (26). In other words, as the crevice surface becomes less hydrophobic (smaller α), the vapor nucleus recedes to the apex of the crevice and is less likely to cavitate, which agrees with the experimental investigations about the effect of material hydrophobicity on the cavitation threshold [3,96]. For real particles in liquid, there are many crevices with various wettabilities and geometries. These crevices have different cavitation thresholds. As a result, the cavitation threshold (the largest P_{liquid} to induce cavitation) is decided by the narrowest and most hydrophobic crevice. The overall cavitation intensity increases with decreasing liquid pressure (more nucleation sites are triggered).
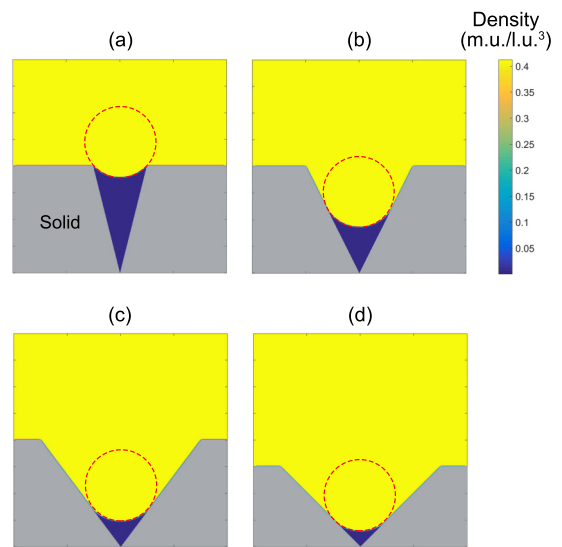

FIG. 10. The effect of crevice shape (β) on vapor nuclei, $\alpha = 170°$, $P_{\text{liquid}} = 3.66 \times 10^{-4}$ m.u. l.u.$^{-1}$ t.s.$^{-2}$. (a) $\beta = 14.03°$; (b) $\beta = 26.55°$; (c) $\beta = 36.87°$; (d) $\beta = 45°$.

A comprehensive comparison of W under stable state is made between simulation results and theoretical values, as shown in Fig. 12. The simulation results are found to match very well with the theoretical values for different crevice shapes. Whether the vapor nucleus is close to the crevice apex (small W) or to the crevice mouth (large W), the maximum difference of W between simulation and theory is less than 1 l.u. Comparison with different wettability (β) is also conducted, and the result is very similar to Fig. 12. As can be seen in Eq. (26), the decrease of α will have the same effect as increasing β. The ability of SCMP LBM to simulate crevice cavitation nucleation is quantitatively verified.
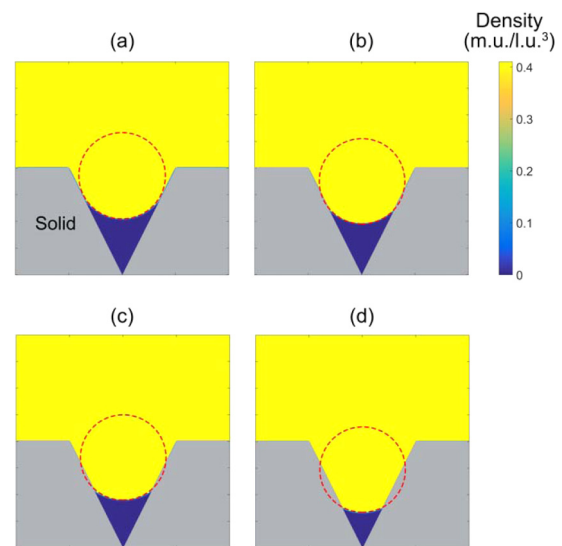

FIG. 11. The effect of crevice surface wettability (α) on vapor nuclei, $\beta = 26.55°$, $P_{\text{liquid}} = 2.54 \times 10^{-4}$ m.u. l.u.$^{-1}$ t.s.$^{-2}$. (a) $\alpha = 170°$; (b) $\alpha = 163°$; (c) $\alpha = 153°$; (d) $\alpha = 145°$.
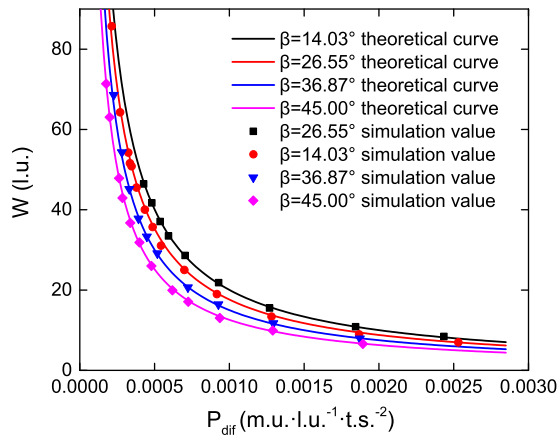
FIG. 12. The comparison of W between simulation results and theoretical values, $\alpha = 170°$.

curve of liquid and vapor matches well with Maxwell construction results, and the numerical surface tension perfectly obeys the Laplace law. The contact angle is found to be lineally related to the adsorption coefficient. The numerical advantages of the present model are demonstrated. The free bubble and crevice cavitation nucleation models are accurately simulated. The existence of critical radius for a seed bubble to cavitate is numerically testified, and the radius evolutions of a free cavitation bubble well match the solutions of the two-dimensional Rayleigh-Plesset equation. Crevices with different shape and wettability have been considered. A narrower crevice with more hydrophobic surface is more favorable for cavitation, and the simulated interface widths are in good accordance with the theoretical calculations. The simulations show excellent agreement with the heterogeneous nucleation theories both in qualitative and in quantitative ways. The applications of the modified SCMP LBM to more complex cavitation problems and multiphase flows is very promising.

V. CONCLUSION

A modified Shan-Chen pseudopotential single-component multiphase lattice Boltzmann method is successfully employed to investigate the free bubble and crevice heterogeneous nucleation models. By using Carnahan–Starling real-gas equation of state, a redefined effective mass function, and the exact difference method forcing scheme, this SCMP LBM can achieve much larger density ratio, better thermodynamic consistency, and numerical accuracy. The simulated coexistence

ACKNOWLEDGMENTS

[1] J.-P. Franc and J.-M. Michel, *Fundamentals of Cavitation*, Fluid Mechanics and Its Applications Vol. 76 (Springer Netherlands, Rotterdam, 2006).

[2] C. E. Brennen, *Cavitation and Bubble Dynamics* (Cambridge University Press, New York, 2013).

[3] B. M. Borkent, S. Gekle, A. Prosperetti, and D. Lohse, Phys. Fluids **21**, 102003 (2009).

[4] D. De Lange and G. De Bruin, in *In Fascination of Fluid Dynamics*, edited by A. Biesheuvel and G. v. Heijst (Springer Netherlands, Dordrecht, 1998), p. 91.

[5] C. Stanley, T. Barber, B. Milton, and G. Rosengarten, Exp. Fluids **51**, 1189 (2011).

[6] M. Dular, I. Khlifa, S. Fuzier, M. A. Maiga, and O. Coutier-Delgosha, Exp. Fluids **53**, 1233 (2012).

[7] P. Kumar and R. Saini, Renewable Sustainable Energy Rev. **14**, 374 (2010).

[8] R. E. Arndt, Annu. Rev. Fluid Mech. **13**, 273 (1981).

[9] L. Gensheng, S. Zhonghou, Z. Changshan, Z. Debin, and C. Hongbing, Petr. Sci. Technol. **23**, 1 (2005).

[10] B. Schneider, A. Koşar, C.-J. Kuo, C. Mishra, G. S. Cole, R. P. Scaringe, and Y. Peles, J. Heat Transfer **128**, 1293 (2006).

[11] P. R. Gogate, Adv. Environ. Res. **6**, 335 (2002).

[12] H. Soyama, T. Kikuchi, M. Nishikawa, and O. Takakuwa, Surf. Coat. Technol. **205**, 3167 (2011).

[13] S. Hattori and N. Mikami, Wear **267**, 1954 (2009).

[14] H. Soyama, Wear **297**, 895 (2013).

[15] K.-H. Kim, G. Chahine, J.-P. Franc, and A. Karimi, *Advanced Experimental and Numerical Techniques for Cavitation Erosion Prediction*, Fluid Mechanics and Its Applications Vol. 106 (Springer Netherlands, Dordrecht, 2014).

[16] R. Watanabe, K. Yanagisawa, T. Yamagata, and N. Fujisawa, Wear **358**, 72 (2016).

[17] E. Hutli, M. S. Nedeljkovic, A. Bonyár, and D. Légrády, Exp. Therm. Fluid Sci. **80**, 281 (2017).

[18] C. Peng, S. Tian, and G. Li, Ocean Eng. **149**, 1 (2018).

[19] M. S. Plesset and A. Prosperetti, Annu. Rev. Fluid Mech. **9**, 145 (1977).

[20] E. Samiei, M. Shams, and R. Ebrahimi, Eur. J. Mech. B **30**, 41 (2011).

[21] M. Sussman, J. Comput. Phys. **187**, 110 (2003).

[22] C.-Y. Hsu, C.-C. Liang, A.-T. Nguyen, and T.-L. Teng, Ocean Eng. **81**, 29 (2014).

[23] S.-W. Chau, K.-L. Hsu, J.-S. Kouh, and Y.-J. Chen, J. Marine Sci. Technol. **8**, 147 (2004).

[24] G. Peng and S. Shimizu, J. Hydrodyn. B **25**, 502 (2013).

[25] B.-B. Li, W. Jia, H.-C. Zhang, and J. Lu, Shock Waves **24**, 317 (2014).

[26] P. Guoyi, Y. Congxin, Y. Oguma, and S. Shimizu, J. Hydrodyn. B **28**, 986 (2016).

[27] F. Magaletti, M. Gallo, L. Marino, and C. M. Casciola, Int. J. Multiphase Flow **84**, 34 (2016).

[28] Y. Liu, A. Zhang, and Z. Tian, Ocean Eng. **75**, 46 (2014).

[29] A. Aganin, M. Ilgamov, L. Kosolapova, and V. Malakhov, Thermophys. Aeromech. **23**, 211 (2016).

[30] A. M. Zhang and Y. L. Liu, J. Comput. Phys. **294**, 208 (2015).

[31] G. L. Chahine and C.-T. Hsiao, Interface Focus **5**, 20150016 (2015).

[32] A. K. Singhal, M. M. Athavale, H. Y. Li, and Y. Jiang, J. Fluids Eng. **124**, 617 (2002).

[33] G. H. Schnerr and J. Sauer, in *Proceedings of Fourth International Conference on Multiphase Flow*, edited by N. Thomas (Elsevier, New York, 2002).

[34] P. J. Zwart, A. G. Gerber, and T. Belamri, in *Proceedings of Fifth International Conference on Multiphase Flow*, edited by Y. Matsumoto (ICMF, Tsukuba, 2004).

[35] S. Succi, *The Lattice Boltzmann Equation: For Fluid Dynamics and Beyond* (Oxford University Press, Oxford, 2001).

[36] M. C. Sukop and D. T. Thorne Jr., *Lattice Boltzmann Modeling: An Introduction for Geoscientists and Engineers* (Springer, Berlin, 2006).

[37] P. Yuan and L. Schaefer, Phys. Fluids **18**, 042101 (2006).

[38] L. Chen, Q. Kang, Y. Mu, Y.-L. He, and W.-Q. Tao, Int. J. Heat Mass Transfer **76**, 210 (2014).

[39] H. Huang, M. C. Sukop, and X. Lu, *Multiphase Lattice Boltzmann Methods: Theory and Application* (John Wiley & Sons, Chichester, 2015).

[40] S. Chen and G. D. Doolen, Annu. Rev. Fluid Mech. **30**, 329 (1998).

[41] A. K. Gunstensen, D. H. Rothman, S. Zaleski, and G. Zanetti, Phys. Rev. A **43**, 4320 (1991).

[42] D. Grunau, S. Chen, and K. Eggert, Phys. Fluids A **5**, 2557 (1993).

[43] M. R. Swift, W. R. Osborn, and J. M. Yeomans, Phys. Rev. Lett. **75**, 830 (1995).

[44] T. Inamuro, N. Konishi, and F. Ogino, Comput. Phys. Commun. **129**, 32 (2000).

[45] G. Falcucci, S. Ubertini, C. Biscarini, S. Di Francesco, D. Chiappini, S. Palpacelli, A. De Maio, and S. Succi, Commun. Comput. Phys. **9**, 269 (2011).

[46] X. He, S. Chen, and R. Zhang, J. Comput. Phys. **152**, 642 (1999).

[47] X. He and G. D. Doolen, J. Stat. Phys. **107**, 309 (2002).

[48] X. Shan and H. Chen, Phys. Rev. E **47**, 1815 (1993).

[49] X. Shan and H. Chen, Phys. Rev. E **49**, 2941 (1994).

[50] M. Sbragaglia, R. Benzi, L. Biferale, S. Succi, K. Sugiyama, and F. Toschi, Phys. Rev. E **75**, 026702 (2007).

[51] Z. Yu and L.-S. Fan, Phys. Rev. E **82**, 046708 (2010).

[52] A. L. Kupershtokh, D. A. Medvedev, and D. I. Karpov, Comput. Math. Appl. **58**, 965 (2009).

[53] H. Huang, M. Krafczyk, and X. Lu, Phys. Rev. E **84**, 046710 (2011).

[54] Q. Li, K. H. Luo, and X. J. Li, Phys. Rev. E **86**, 016709 (2012).

[55] K. Sun, T. Wang, M. Jia, and G. Xiao, Phys. A (Amsterdam) **391**, 3895 (2012).

[56] Q. Li, K. H. Luo, and X. J. Li, Phys. Rev. E **87**, 053301 (2013).

[57] M. C. Sukop and D. Or, Phys. Rev. E **71**, 046703 (2005).

[58] S. K. Mishra, P. Deymier, K. Muralidharan, G. Frantziskonis, S. Pannala, and S. Simunovic, Ultrason. Sonochem. **17**, 258 (2010).

[59] X. Chen, Commun. Comput. Phys. **7**, 212 (2010).

[60] S. Gong and P. Cheng, Int. J. Heat Mass Transfer **55**, 4923 (2012).

[61] S. Gong and P. Cheng, Int. J. Heat Mass Transfer **64**, 122 (2013).

[62] G. Falcucci, E. Jannelli, S. Ubertini, and S. Succi, J. Fluid Mech. **728**, 362 (2013).

[63] G. Falcucci, S. Ubertini, G. Bella, and S. Succi, Commun. Comput. Phys. **13**, 685 (2013).

[64] D. Mahdi, T.-R. Mohammad, and M. Hamidreza, Chin. Phys. B **24**, 024302 (2015).

[65] G. Kähler, F. Bonelli, G. Gonnella, and A. Lamura, Phys. Fluids **27**, 123307 (2015).

[66] J. Yang, Z. Shen, X. Zheng, and L. Li, J. Appl. Math. Phys. **3**, 947 (2015).

[67] M.-l. Shan, C.-p. Zhu, Z. Xi, Y. Cheng, and Q.-B. Han, J. Hydrodyn. B **28**, 442 (2016).

[68] M.-L. Shan, C.-P. Zhu, C. Yao, C. Yin, and X.-Y. Jiang, Chin. Phys. B **25**, 104701 (2016).

[69] V. Sofonea, T. Biciusca, S. Busuioc, V. E. Ambrus, G. Gonnella, and A. Lamura, Phys. Rev. E **97**, 023309 (2018).

[70] X.-P. Chen, C.-W. Zhong, and X.-L. Yuan, Comp. Math. Appl. **61**, 3577 (2011).

[71] Z. Guo and C. Shu, *Lattice Boltzmann Method and Its Applications in Engineering*, Advances in Computational Dynamics Vol. 3 (World Scientific, Singapore, 2013).

[72] T. Krüger, H. Kusumaatmaja, A. Kuzmin, O. Shardt, G. Silva, and E. M. Viggen, *The Lattice Boltzmann Method* (Springer International Publishing, Cham, 2017).

[73] L. J. Briggs, J. Appl. Phys. **21**, 721 (1950).

[74] Q. Zheng, D. Durben, G. Wolf, and C. Angell, Science **254**, 829 (1991).

[75] E. N. Harvey, A. Whiteley, W. McElroy, D. Pease, and D. Barnes, J. Cell. Comp. Physiol. **24**, 23 (1944).

[76] R. E. Apfel, J. Acoust. Soc. Am. **48**, 1179 (1970).

[77] A. A. Atchley and A. Prosperetti, J. Acoust. Soc. Am. **86**, 1065 (1989).

[78] M. Arora, C.-D. Ohl, and K. A. Mørch, Phys. Rev. Lett. **92**, 174501 (2004).

[79] K. A. Mørch, Phys. Fluids **19**, 072104 (2007).

[80] Y. Qian, D. d'Humières, and P. Lallemand, Europhys. Lett. **17**, 479 (1992).

[81] X. Shan, Phys. Rev. E **73**, 047701 (2006).

[82] N. S. Martys and H. Chen, Phys. Rev. E **53**, 743 (1996).

[83] Z. Yang, T.-N. Dinh, R. Nourgaliev, and B. Sehgal, Int. J. Heat Mass Transfer **44**, 195 (2001).

[84] D. Or and M. Tuller, Water Resour. Res. **38** (2002).

[85] L. Rayleigh, London Edinburgh Dublin Phil. Mag. J. Sci. **34**, 94 (1917).

[86] M. S. Plesset, J. Appl. Mech. **16**, 277 (1949).

[87] Q. Zou and X. He, Phys. Fluids **9**, 1591 (1997).

[88] E. Gates and J. Bacon, J. Ship Res. **22**, 29 (1978).

[89] J. Katz, Division of Engineering and Applied Science, California Institute of Technology, Report (1978).

[90] D. E. Yount, J. Acoust. Soc. Am. **65**, 1429 (1979).

[91] D. E. Yount, J. Acoust. Soc. Am. **71**, 1473 (1982).

[92] S. Huang, A. Ihara, H. Watanabe, and H. Hashimoto, J. Fluids Eng. **118**, 749 (1996).

[93] C. Haosheng, W. Jiadao, and C. Darong, Wear **266**, 345 (2009).

[94] D. Yan, J. Wang, and F. Liu, AIP Advances **5**, 077159 (2015).

[95] L. Crum and J. Brosey, J. Fluids Eng. **106**, 99 (1984).

[96] B. M. Borkent, M. Arora, and C.-D. Ohl, J. Acoust. Soc. Am. **121**, 1406 (2007).